

# Observation of Rashba-Surface-Band-Dependent Yu–Shiba–Rusinov States in a Gold-Based Superconductor AuSn<sub>4</sub>

Zichen Huang,<sup>⊥</sup> Hui Chen,<sup>\*,⊥</sup> Rui Song,<sup>⊥</sup> Hui Guo,<sup>⊥</sup> Hao Zhang, Guoyu Xian, Senhao Lv, Guangyuan Han, Ruisong Ma, Geng Li, Chengmin Shen, Haitao Yang, Qing Huan, and Hong-Jun Gao<sup>\*</sup>



Cite This: *Nano Lett.* 2025, 25, 5375–5382



Read Online

ACCESS |

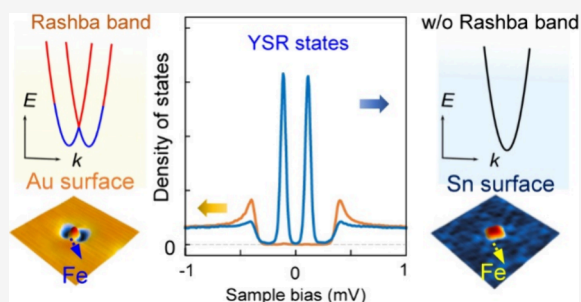
Metrics & More

Article Recommendations

Supporting Information

**ABSTRACT:** The interplay between the Rashba effect, superconductivity, and magnetism in gold-based superconductors provides a platform for exploring topological superconductivity, yet the interaction between Rashba bands and superconducting bound states remains unexplored. Here, we report Rashba-surface-band-dependent Yu–Shiba–Rusinov (YSR) states around Fe adatoms on the surfaces of AuSn<sub>4</sub>, using ultralow temperature (5 mK) scanning tunneling microscope/spectroscopy. On Au-terminated surfaces with Rashba bands, most Fe atoms occupy Au vacancies, while only a few adsorb on the Sn-terminated surfaces with dominant bulk metallic states. Remarkably, YSR states localized on the Fe atom are observed on Sn-terminated surfaces but absent on Au-terminated surfaces. First-principle calculations reveal a significant magnetic moment for Fe adatoms on Sn surfaces compared to a nearly negligible value on Au surfaces, which elucidates the observed surface-dependent YSR states. The termination-dependence local moment arises from the interplay of Rashba surface bands and *s-d* coupling, as described by the Anderson *s-d* exchange model.

**KEYWORDS:** *Magnetic adatoms, Yu–Shiba–Rusinov states, superconductors, noble metal, Rashba band, scanning tunneling microscopy/spectroscopy*



The interplay between spin–orbit coupling (SOC), superconductivity, and magnetism has captured significant interest for its potential to realize topological superconductivity and host Majorana zero modes.<sup>1–3</sup> A widely used approach involves constructing a hybrid system of superconductivity combining with the materials with SOC<sup>4,5</sup> or magnetism.<sup>6,7</sup> These heterostructures not only facilitate symmetry breaking, which is essential for Rashba SOC,<sup>8,9</sup> but also enable the tailoring of proximity effects, where the emergent physics of the system exceeds the sum of its constituents. While these hybrid systems have been extensively studied, intrinsic superconductors with strong SOC<sup>10,11</sup> offer a simpler and potentially more robust platform for investigating the interplay of unconventional surface states and magnetic impurities. In particular, the Yu–Shiba–Rusinov (YSR) states induced by the interaction between localized impurity spins and superconducting quasiparticles<sup>12–14</sup> have long served as powerful probes of the pairing symmetry and SOC effects in such systems.<sup>15–18</sup> However, the correlation between Rashba band splitting and magnetic impurity states in intrinsic superconductors remains largely unexplored, posing a significant challenge for understanding these materials.

Gold-based materials have emerged as a promising platform for studying strong SOC<sup>19,20</sup> and its interplay with superconductivity.<sup>21–23</sup> The Shockley surface state (SS) of Au(111) is a well-known example, featuring strong Rashba SOC that has

recently been predicted to exhibit a topological nature.<sup>24</sup> Beyond surface states, gold-based superconductors such as Au film/superconductors heterostructures<sup>25–29</sup> and AuPb<sub>2</sub><sup>30</sup> have been recently explored for their topological band and possible topological superconductivity. Among these materials, AuSn<sub>4</sub> has garnered particular attention as a noble metal alloy combining strong SOC with intrinsic superconducting states.<sup>31–34</sup> Robust zero-energy vortex bound states and unconventional Rashba-split band structures with the same spin textures have been reported in AuSn<sub>4</sub>.<sup>35,36</sup> Therefore, AuSn<sub>4</sub> serves as a promising platform for investigating the interplay of SOC, topology, and superconductivity. However, the interaction between magnetic impurities and Rashba bands in AuSn<sub>4</sub> remains unexplored.

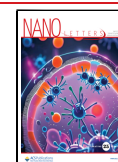
Here, we report the Rashba-surface-band-dependent YSR states on the iron atoms embedded in the AuSn<sub>4</sub> crystal by utilizing scanning tunneling microscope/spectroscopy at an ultralow temperature of 5 mK (with an effective electronic temperature of 138 mK, Figure S8). We deposited Fe atoms on

**Received:** January 23, 2025

**Revised:** March 18, 2025

**Accepted:** March 20, 2025

**Published:** March 24, 2025



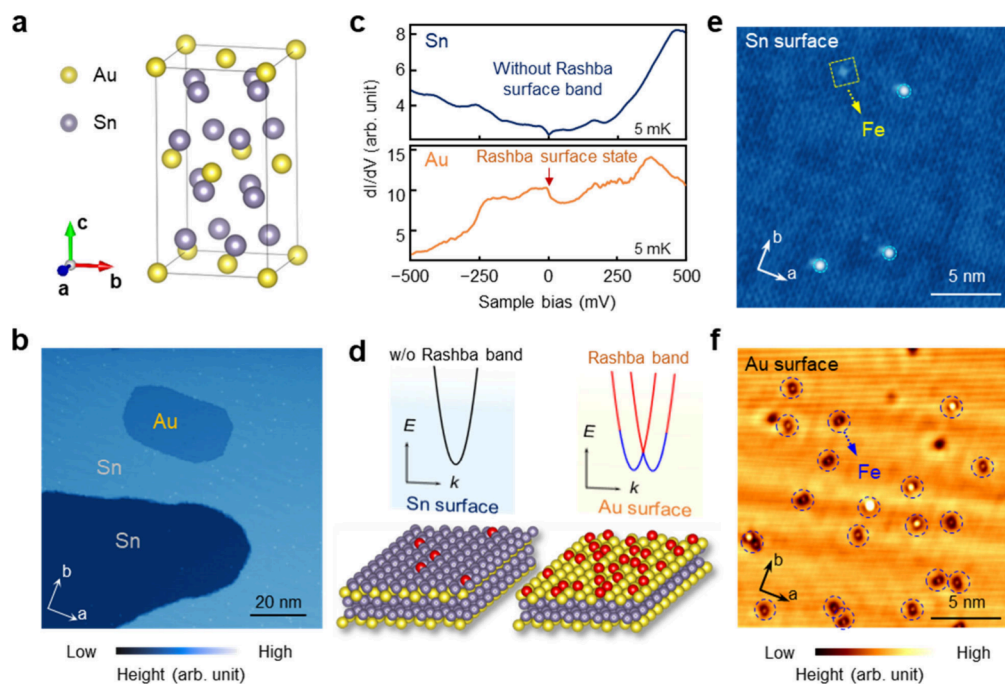


**Figure 1.** Fe atoms on the Au and Sn terminated surfaces of  $\text{AuSn}_4$  crystal. (a) Schematic showing the crystal structure of  $\text{AuSn}_4$ . (b) Large-scale STM image of cleaved  $\text{AuSn}_4$  surface, showing Sn- and Au-terminated surfaces ( $V_s = -0.5$  V,  $I_t = 50$  pA). (c) Comparison of spatially averaged  $dI/dV$  spectra on Sn surface and Au surface; the unconventional Rashba bands are dominant at Au surfaces, leading to higher DOS at the Fermi level ( $V_s = -500$  mV,  $I_t = 1$  nA,  $V_{\text{mod}} = 2$  mV). (d) Schematic model showing the Au and Sn surface of  $\text{AuSn}_4$  after Fe deposition; the corresponding band structures for each surface are indicated. (e) STM image of typical Fe-deposited Sn surface with two kinds of adatoms, where the majority adatoms are marked with cyan circles, and the minority adatom is marked with a yellow square ( $V_s = -10$  mV,  $I_t = 1$  nA). (f) STM image of typical Fe-deposited Au surface with multiple adatoms, marked with blue dashed circles ( $V_s = -10$  mV,  $I_t = 1$  nA).

the cleaved surface of  $\text{AuSn}_4$ . On Au-terminated surfaces with a pronounced Rashba surface state, the Fe atoms are trapped inside surface vacancies as interstitial impurities, showing no signature of local magnetic moment. In contrast, the Fe atoms adsorbed at the Sn surface as adatoms. Intriguingly, we observe a pronounced pair of particle–hole symmetric in-gap bound states upon the Fe adatoms of Sn surfaces. The in-gap states energy can be tuned by varying the exchange coupling, which are attributed to the YSR states. The different behaviors of Sn surfaces and Au surfaces toward magnetic impurities can be well explained by the simple Anderson  $s$ - $d$  exchange model. The large density of states at the Fermi level that originate from the unconventional Rashba bands and the strong  $s$ - $d$  coupling between Fe adatoms and Au surfaces result in the nonmagnetic localized impurity state of Fe adatoms. Density functional theory calculations further confirm this assumption, with the effective magnetic moment of Fe adatoms being  $2.6 \mu_B$  on Sn surfaces and  $0.05 \mu_B$  on Au surfaces. Our findings underscore the potential of  $\text{AuSn}_4$  as a platform for investigating the interplay of SOC, topology, and superconductivity.

$\text{AuSn}_4$  possesses an orthorhombic crystal structure and belongs to space group  $Aba2$  ( $a = b = 6.476$  Å,  $c = 11.666$  Å, Figure 1(a)). The periodic stacking of Sn–Au–Sn trilayers results in two possible cleaved surfaces: Au- and Sn-terminated surfaces. A large-scale STM image shows a typical cleaved surface of  $\text{AuSn}_4$  with multiple layers (Figure 1(b)), and Sn- and Au-terminated surfaces can be determined by the height differences between adjacent layers. The height differences are  $\sim 0.62$  nm between adjacent Sn layers and  $\sim 0.18$  nm between adjacent Sn and Au layers, and the majority of cleaved surfaces are Sn terminated while Au-terminated surfaces are rarely

observed (Figure S1). It has been demonstrated that  $\text{AuSn}_4$  possesses unconventional Rashba bands and is mainly distributed on Au surfaces (Figure 1(c)).<sup>36</sup> The differential conductance ( $dI/dV$ ) spectra of the Au-terminated surface show broad peaks around Fermi surfaces which are attributed to the unconventional Rashba band, while Sn surfaces exhibit metallic bulk states (Figure 1(c)).

The Fe atoms show distinct adsorption features at the terminations with various surface states (Figure 1(d)). Before deposition, some native adatoms with a height of 0.15 nm already exist on the Sn surface (cyan circles in Figure 1(e)).<sup>31,36</sup> After deposition, very few adatoms with a lower height than native adatoms (0.05 nm in height) are observed on the Sn surface, which are identified as Fe adatoms (yellow square in Figure 1(e)). In contrast, there are no adatoms but some native vacancies on pristine Au surfaces.<sup>36</sup> After deposition, the density of vacancies on the Au surface increases significantly, and a large amount of Fe atoms are embedded inside the vacancies (Figure 1(f); comparison of Au surfaces with/without Fe deposition is shown in Figure S2). Such features are similar to the interstitial impurities in iron-based superconductors.<sup>37</sup> A rough estimation based on cumulative counts within areas imaged with high resolution shows that the defect density of Fe atoms on Au surfaces ( $43 \times 10^{11} \text{ cm}^{-2}$ ) are much higher than that on Sn surfaces ( $0.05 \times 10^{11} \text{ cm}^{-2}$ ), despite that the Sn-terminated surfaces are most common after cleaving.<sup>36</sup> It indicates that the Fe atoms on Au- and Sn-terminated surfaces may exhibit distinct electronic states.

We then investigate the detailed structural features and local density of states (DOS) around the Fe impurities on the Au surface. The Fe atoms are trapped inside the vacancies with various heights, as shown in Figure 2(a). Regarding the height

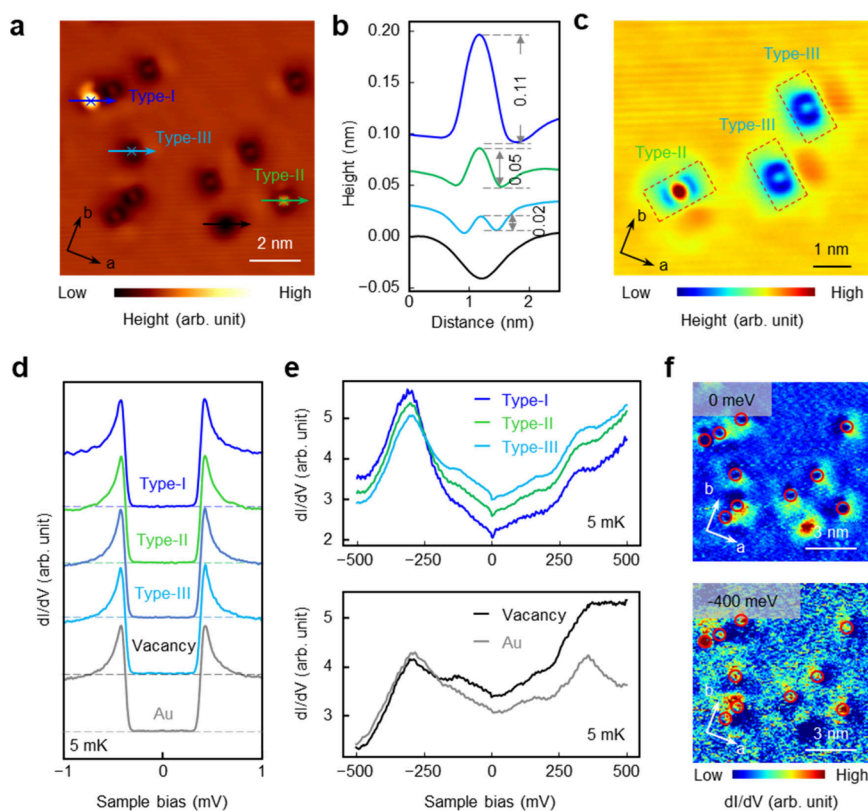


**Figure 2.** Absence of local magnetic moment and reduction of Rashba surface states induced by the Fe impurities on the Au surface. (a) STM image of Au surface after Fe deposition; three different types of impurities and vacancy are marked in orange, green, red, and black squares, respectively ( $V_s = -0.5$  V,  $I_t = 1$  nA). (b) Height profile measured on Fe impurities and vacancy marked in (a). A significant height difference can be found in different types of impurities, and the profiles are offset for clarity. (c) Detailed STM image of Fe impurities showing  $C_2$  local symmetry, as indicated by red rectangles; the two symmetrical axes are  $45^\circ$  to  $a$  and  $b$  crystal axis ( $V_s = -0.5$  V,  $I_t = 1$  nA). (d) The  $dI/dV$  spectra measured on three types of Fe impurities together with the spectra measured on vacancy and Au background, showing the absence of YSR states. The spectra are offset for clarity ( $V_s = -1$  mV,  $I_t = 1$  nA,  $V_{\text{mod}} = 10$   $\mu$ V). (e) Comparison of  $dI/dV$  spectra with a wider energy range ( $V_s = -0.5$  V,  $I_t = 1$  nA,  $V_{\text{mod}} = 2$  mV). (f) The  $dI/dV$  maps at 0 meV (upper panel) and  $-400$  meV (lower panel) of the same area in (a). The Fe impurities are marked by cyan circles ( $V_s = -0.5$  V,  $I_t = 1$  nA,  $V_{\text{mod}} = 5$  mV).

profile, the Fe impurities are classified into three types, which are labeled as Types I, II, and III, respectively (Figure 2(b)). Type I impurities are the highest (height is about 0.11 nm), while Types II and III impurities are halfway (height is about 0.05 nm) and completely embedded (height is about 0.02 nm) into Au substrate, respectively. Such classification is further confirmed by the statistical topographic data on a large-scale Au surface (Figure S3). All three types of impurities show a local  $C_2$  symmetric feature with an elongated axis along a direction rotated  $45^\circ$  with a crystalline axis (Figure 2(c)). It should be noted that the crystalline Au lattice around Fe impurities is difficult to be resolved due to the strong quasiparticle interferences.

Considering the magnetism of Fe, the Kondo effect<sup>38</sup> or YSR states<sup>39</sup> can be expected when the magnetic moment interacts with a metallic superconductor such as AuSn<sub>4</sub>. We collect low-energy  $dI/dV$  spectra on the Fe impurities of Au surfaces, which are proportional to DOS near the Fermi level. Surprisingly, the  $dI/dV$  spectra on three types of Fe impurities show U-shaped hard SC gaps without any signature of YSR states (Figure 2(d)), being completely the same as that of Fe-free vacancies and bare Au surfaces. In order to study the impact of Fe impurities on the surface bands of Au surfaces, we obtain larger-scale  $dI/dV$  spectra on all of the Fe impurities as shown in Figure S3(b). Averaged spectra of each type of

impurities, together with averaged spectra on Fe-free vacancy and bare Au surfaces, are shown in Figure 2(e). For Fe impurities, the peak at the Fermi level (Figure S4), which corresponds to the unconventional Rashba surface states,<sup>36</sup> is suppressed, while the one in the vicinity of  $-350$  meV corresponding to the conventional Rashba band<sup>36</sup> is enhanced. The above trends are visible in the  $dI/dV$  map measured at the Fermi level and at  $-400$  meV (Figure 2(f)). A reduction of the DOS is observed only on the center of Fe impurities at the Fermi level, while an enhancement is observed at  $-400$  meV. In addition, no Kondo resonance is observed at a large energy range. The absence of a local moment is repeatable for all of the Fe impurities of Au surfaces.

In contrast to the absence of a local moment on the Au surface, the Fe adatoms on Sn surfaces exhibit pronounced bound states inside the superconducting gap. The atomically resolved STM image shows that Fe adatoms are located in the center of the square formed by Sn atoms in one unit cell (Figure 3(a)). A comparison of  $dI/dV$  spectra measured on a Fe adatom in Figure 3(a) and on a bare Sn surface is shown in Figure 3(b). Surprisingly, a pair of pronounced conductance peaks are observed on the Fe adatom, with peaks energy located at  $\pm 0.107$  meV, symmetrical to the Fermi level. The  $dI/dV$  linecut measured across Fe along the  $b$  lattice direction shows that the symmetric bound states are localized around Fe

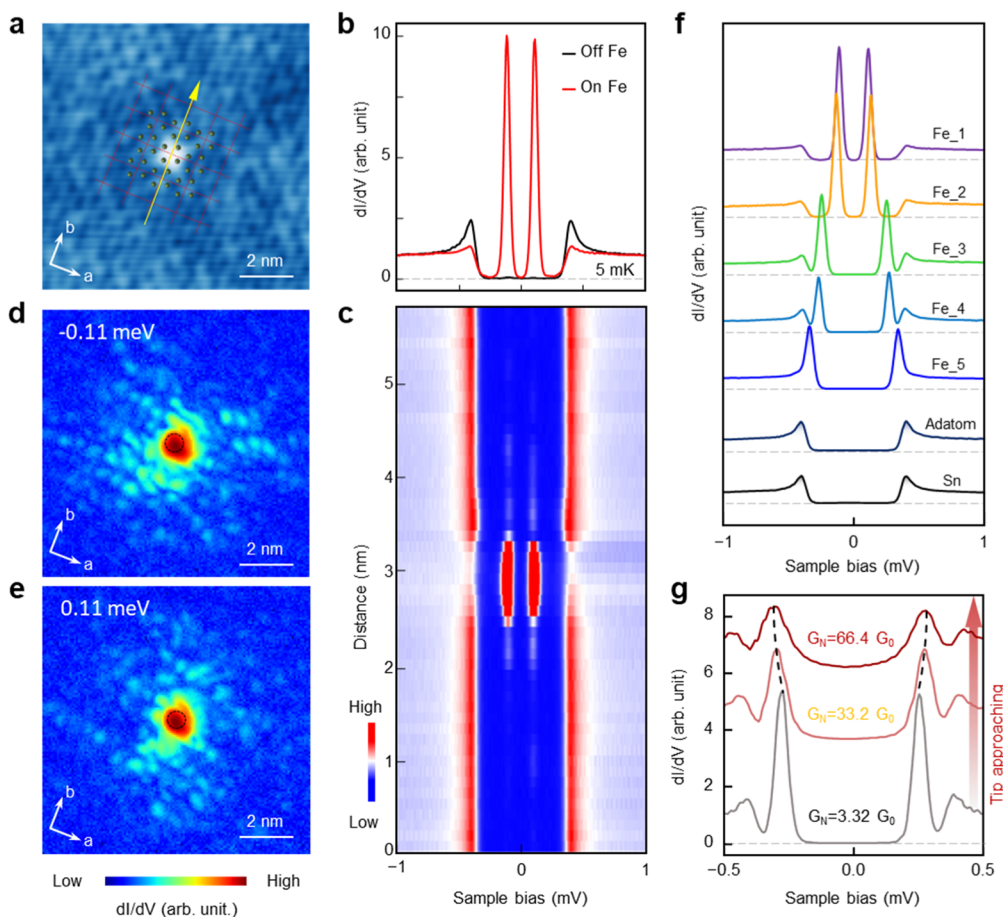


**Figure 3.** Observation of YSR states on the Fe adatoms on the Sn surface. (a) Atomically resolved STM image of Sn surface with single Fe adatom, showing the adsorption site of Fe adatoms. The red dotted grid represents the position of unit cells, and the crystal model of the Sn layer is overlaid ( $V_s = -10$  mV,  $I_t = 100$  pA). (b) The  $dI/dV$  spectra measured on and off the Fe adatom shown in (a), respectively, showing pronounced YSR states on the Fe adatom ( $V_s = -1$  mV,  $I_t = 1$  nA,  $V_{\text{mod}} = 10$   $\mu$ V). (c) The  $dI/dV$  linecut along the yellow arrow in (a) across the Fe adatom shown in (a), showing that the YSR states localized around the Fe adatom ( $V_s = -1$  mV,  $I_t = 1$  nA,  $V_{\text{mod}} = 10$   $\mu$ V). (d, e) The  $dI/dV$  maps at the energies of in-gap states, i.e.,  $-0.11$  meV (d) and  $0.11$  meV (e), showing the spatial distribution of the YSR state around the Fe adatom. The positions of the Fe adatom are marked by a black circle ( $V_s = -1$  mV,  $I_t = 1$  nA,  $V_{\text{mod}} = 50$   $\mu$ V). (f) A series of  $dI/dV$  spectra measured on different Fe adatoms, normal adatom, and Sn background, showing various in-gap states on the Fe adatoms. The spectra are offset for clarity ( $V_s = -1$  mV,  $I_t = 1$  nA, and  $V_{\text{mod}} = 10$   $\mu$ V). (g) A series of  $dI/dV$  spectra of Fe\_3 atoms in (f) measured under different tip–sample distance, showing that the energy positions of YSR peaks shift closer to the coherence peak with increasing tunneling conductance, as indicated by black dashed lines (tunneling conductance for each spectrum is marked in units of  $G_0 = 2e^2/h \times 10^{-3}$ ).

adatoms (Figure 3c), which are absent at native adatoms (Figure S5(a)). We attribute the in-gap bound states to the YSR states induced by the local moment of Fe adatoms. The YSR states show a long-range falloff of the intensity (Figure 3(c)).

To study the real-space distribution of the YSR states, we collect  $dI/dV$  maps inside the superconducting gap. The  $dI/dV$  maps at the peak energies show an inhomogeneous spatial oscillation pattern extending 5 nm from the adatom (Figure 3(d, e) and Figure S9)). In contrast, at the energies beyond the superconducting gap, the  $dI/dV$  maps show a reduced DOS localized at the Fe adatom without electronic interference (Figure S6). Thus, the oscillation pattern is a characteristic feature of YSR states, indicating an asymmetric orbital shape of the scattering potential<sup>40</sup> and anisotropic Fermi surface.<sup>41</sup>

The YSR states for the Fe adatoms (for details, see Figures S5 and S7) at Sn surfaces are systematically studied, and it is found that throughout the whole sample surface the YSR states are different. The series of Fe adatoms in various surface regions present different kinds of particle–hole symmetric in-

gap states (Figure 3(f)). The lower the energy of the in-gap states sit, the stronger intensity they present. These various in-gap states arise from the change of exchange coupling between different Fe adatoms and AuSn<sub>4</sub> substrates.<sup>42–44</sup> The bound states close to the Fermi level are located near the quantum phase transition point of the YSR states. To confirm this, we perform  $G_N$ -dependent  $dI/dV$  measurements for the Fe\_3 atoms. With increasing  $G_N$ , the in-gap states move away from zero energy and approach close to the coherence peaks, further supporting that the in-gap states on the Fe adatoms are YSR states (Figure 3(g)).

From the above experimental results, Fe impurities on Au surfaces show no sign of local moments, while pronounced YSR states are observed on the Fe adatoms on the Sn surfaces. The dramatic differences are explained qualitatively by the Anderson  $s$ - $d$  exchange model,<sup>45</sup> which emphasizes the exchange effect between localized  $d$  electron with itinerant  $s$  electrons. When an Fe atom is merged into a nonmagnetic metallic substrate, it can no longer be considered as an isolated magnetic atom, and the Hamiltonian should be written as

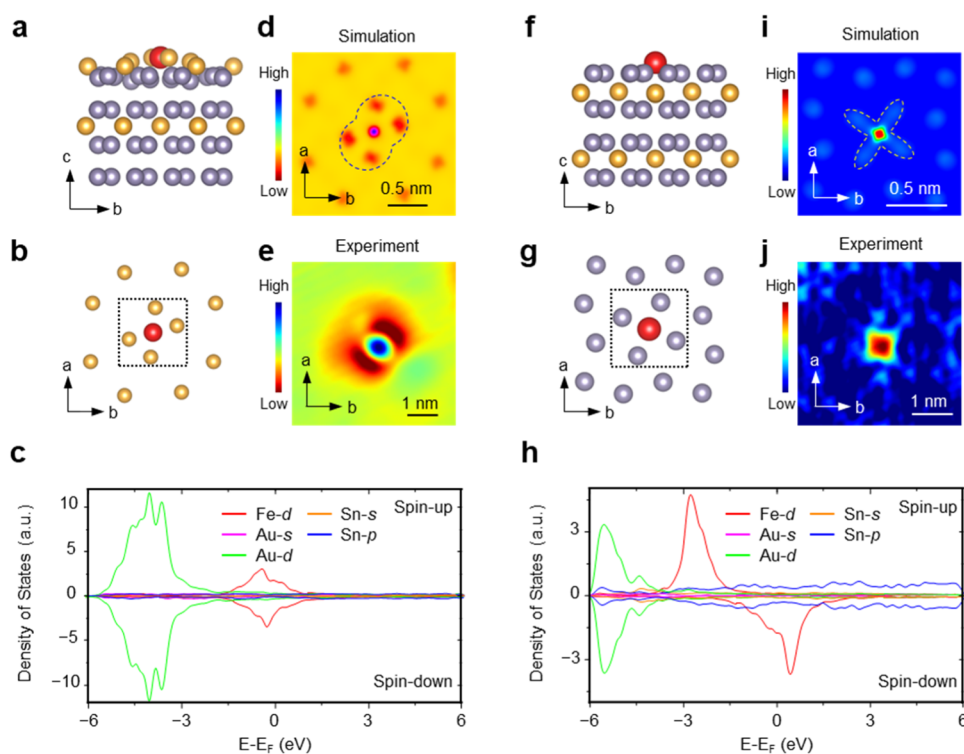


**Figure 4.** Calculated structural configurations and electronic states of the Fe atoms on Au- and Sn-terminated surfaces. (a, b) Side view (a) and top view (b) of calculated structural configuration of Fe atom on Au surface, showing that the Fe atom is embedded within the Au layer. The unit cell is indicated by a black dashed square. (c) Spin-dependent DOS of the Fe impurities on the Au surface, showing an effective magnetic moment of  $0.05 \mu_B$  per Fe adatom. (d) Simulated STM image by integrating the DOS of Fe atoms, showing a  $C_2$  pattern around the embedded Fe impurity (highlighted by the blue dotted lines). (e) STM image of the Fe impurity on Au surface, showing a similar  $C_2$  pattern with a calculated structural configuration. (f, g) Side view (f) and top view (g) of calculated structural configuration of Fe atom on Sn surface, showing that the Fe atom adsorbs above Sn layer. The unit cell is indicated by a black dashed square. (h) Spin-dependent DOS of the Fe adatoms on the Sn surface, showing an effective magnetic moment of  $2.6 \mu_B$  per Fe adatom. (i) Simulated STM image by integrating the DOS of Fe atoms, showing a  $C_4$  pattern around the Fe adatom (highlighted by the yellow dotted lines). (j) STM image of the Fe impurity on a Sn surface, exhibiting a similar  $C_4$  pattern with a calculated structural configuration.

$$H = \sum_{k,\sigma} E_{k\sigma} n_{k\sigma} + \sum_{\sigma} E_d n_{d\sigma} + U n_{\uparrow} n_{\downarrow} + \sum_{k,\sigma} V_{kd} (C_{k\sigma}^+ d_{\sigma} + d_{\sigma}^+ C_{k\sigma})$$

The first and second terms represent the Hamiltonian of itinerant electrons in the metal and the Hamiltonian of  $d$  electron in an isolated Fe atom. The third term represents the correlation effect for the electrons localized on the impurity site where  $U$  denotes the correlation energy. The fourth term describes the exchange coupling between magnetic  $d$  electron in Fe and itinerant electrons in the metal substrate, allowing electrons to hop on and off the impurity site, and the  $V_{kd}$  represents the strength of  $s$ - $d$  exchange. This Hamiltonian leads to a finite width of the impurity level  $\Gamma = \pi V_{kd}^2 \rho_0$ , where  $\rho_0$  is the DOS of the metal substrate at the Fermi level. In Anderson's theory, if  $\Gamma > U/\pi$ , the metallicity of the substrate is so strong that the  $d$  electron of the magnetic impurity will be "delocalized" by the itinerant electrons, resulting in a nonmagnetic ground state. Conversely, if  $\Gamma < U/\pi$ , it means the  $d$  electron is still localized at the impurity site, leading to a magnetic ground state.

In the case of  $\text{AuSn}_4$ , comparing to the Sn surfaces, the Au surfaces have higher DOS at the Fermi level due to the surface states arising from unconventional Rashba bands,<sup>36</sup> and considering the Rashba SOC enhanced  $s$ - $d$  exchange

interaction,<sup>46</sup> a higher  $s$ - $d$  exchange coefficient  $V_{kd}$  is expected for the Fe impurities embedded in Au surfaces. These result in a higher  $\Gamma$  in Au surfaces, much larger than  $U/\pi$ , while in Sn surfaces  $\Gamma < U/\pi$ . As a result, the impurity states on Au surfaces are nonmagnetic, while the impurity states on Sn surfaces are magnetic, which explains the experimental observations of termination-dependent local moment of Fe adatoms.

To provide more quantitative evidence, we perform density functional theory calculations. The calculated optimal adsorption site of Fe atom is embedded within the Au layer (Figure 4(a)). Additionally, the adjacent Au atoms are distorted, and a rectangular structure with  $C_2$  symmetry is formed around the Fe adatom. The orientation of this rectangular structure has two equivalent directions, each at  $45^\circ$  to the  $a$  or  $b$  axis (Figure 4(b)). The calculated spin-polarized DOS of Fe impurities on Au surfaces shows very weak spin dependence, with an effective magnetic moment of  $0.05 \mu_B$  per Fe adatom (Figure 4(c)), with a smaller energy range as shown in Figure S10(a). The nearly negligible value supports the observed absence of YSR states of the Fe impurity on Au surfaces. The simulated STM image by integrating the DOS of Fe atoms shows a  $C_2$  pattern around the embedded Fe impurity (Figure 4(d)), which matches well with the topographic features of Fe impurities at the Au surface in the STM images (Figure 4(e)).

At the Sn surfaces, Fe atoms are adsorbed on the Sn surface (Figure 4(f)). The calculated adsorption site of the Fe atom is at the bridge position of the Sn square lattice (Figures 4(g)). The Fe atoms on Sn surfaces show strong spin-dependent DOS with effective magnetic moments of  $2.6 \mu_B$  per Fe adatom (Figure 4(h)), with a smaller energy range in Figure S10(b)), which further supports the observations of YSR states around Fe adatoms on the Sn surface. The simulated STM image based on the integrated DOS of Fe atoms shows a  $C_4$  pattern (Figure 4(i)), which shows a similar pattern with the topographic features of the Fe adatom of a Sn surface in the STM images (Figure 4(j)).

In summary, we find that the single Fe adatoms reserve their local magnetism at the Sn surfaces, leading to pronounced YSR states, while they lack their local magnetism at the Au surfaces, leading to the absence of any magnetic-related phenomena. The dramatic differences between these two surfaces can be well explained by the basic Anderson *s-d* exchange model and are further confirmed by first-principles calculations. Our work has proven AuSn<sub>4</sub> to be an ideal platform to investigate the interplay of superconductivity with SOC and magnetism in condensed matter physics.

## METHODS

**Single-Crystal Growth of AuSn<sub>4</sub>.** The single crystals of AuSn<sub>4</sub> (space group: *Aba2* No. 41) were synthesized by the self-flux method with excess Sn. The sources are high-purity Au wires (Alfa, 99.999%) and Sn pellets (Alfa, 99.999%) which weighed with a molar ratio of 12:88 in the glovebox. Then, the mixture of the sources was transferred to an alumina crucible and sealed in an evacuated quartz tube. The quartz tube was heated to 850 °C by a box furnace and held for 24 h, followed by cooling to 310 °C for 11 h and then slowly cooled to 230 °C with a rate of 0.5 °C/h. Subsequently, the extra Sn flux is removed by centrifuge at 230 °C. Large AuSn<sub>4</sub> single crystals with a silvery luster were obtained.

**Scanning Tunneling Microscopy/Spectroscopy.** Experiments were performed in an ultrahigh vacuum ( $1 \times 10^{-10}$  mbar) ultralow temperature STM system equipped with external magnetic field perpendicular to the sample surface. The AuSn<sub>4</sub> samples used in the STM/STS experiments were cleaved at room temperature (300 K) in an ultrahigh vacuum chamber, and Fe atoms were immediately *in situ*-deposited on the cleaved surfaces. The samples were then transferred to the STM scanner and cooled to 6 K. The lowest base temperature is 5 mK with an electronic temperature of 138 mK (Figure S8). All the scanning parameters (set point voltage  $V_s$  and tunneling current  $I_t$ ) of the STM topographic images are listed in the figure captions. The *dI/dV* spectra were acquired by a standard lock-in amplifier at a modulation frequency of 877.1 Hz, and the modulation bias ( $V_{mod}$ ) is listed in the figure captions. Nonmagnetic tungsten tips were fabricated via electrochemical etching and calibrated on a clean Au(111) surface prepared by repeated cycles of sputtering with argon ions and annealing at 500 °C.

**DFT Calculations.** First-principles calculations were performed by density functional theory (DFT) using the Vienna ab initio simulation package (VASP).<sup>47,48</sup> The plane-wave basis with an energy cutoff of 380 eV was adopted. The electron–ion interactions were modeled by the projector augmented wave potential (PAW),<sup>49</sup> and the exchange–correlation functional was approximated by the Perdew–Burke–Ernzerhof-type (PBE) generalized gradient approxima-

tion (GGA).<sup>50</sup> The structural relaxation for optimized lattice constants and atomic positions was performed with an energy (force) criterion of  $10^{-8}$  eV (0.01 eV/Å) and by using the DFT-D3<sup>51</sup> method to include van der Waals corrections.

## ASSOCIATED CONTENT

### Supporting Information

The Supporting Information is available free of charge at <https://pubs.acs.org/doi/10.1021/acs.nanolett.5c00523>.

Topographic and spectra characterization of Au and Sn layers, detailed topography of Au surfaces before/after Fe deposition, *dI/dV* spectrum showing the reduction of DOS at Fe impurity on Au surface, more spectra and topographic characterization of YSR states at different Fe adatoms on Sn surface, DFT calculation results at smaller energy range, and determination of the electronic temperature (PDF)

## AUTHOR INFORMATION

### Corresponding Authors

**Hong-Jun Gao** – Beijing National Center for Condensed Matter Physics and Institute of Physics, Chinese Academy of Sciences, Beijing 100190, P. R. China; School of Physical Sciences, University of Chinese Academy of Sciences, Beijing 100190, P. R. China; Hefei National Laboratory, 230088 Hefei, Anhui, P. R. China; [orcid.org/0000-0002-6766-0623](https://orcid.org/0000-0002-6766-0623); Email: [hjgao@iphy.ac.cn](mailto:hjgao@iphy.ac.cn)

**Hui Chen** – Beijing National Center for Condensed Matter Physics and Institute of Physics, Chinese Academy of Sciences, Beijing 100190, P. R. China; School of Physical Sciences, University of Chinese Academy of Sciences, Beijing 100190, P. R. China; Hefei National Laboratory, 230088 Hefei, Anhui, P. R. China; [orcid.org/0000-0002-3369-8113](https://orcid.org/0000-0002-3369-8113); Email: [hchenn04@iphy.ac.cn](mailto:hchenn04@iphy.ac.cn)

### Authors

**Zichen Huang** – Beijing National Center for Condensed Matter Physics and Institute of Physics, Chinese Academy of Sciences, Beijing 100190, P. R. China; School of Physical Sciences, University of Chinese Academy of Sciences, Beijing 100190, P. R. China

**Rui Song** – Science and Technology on Surface Physics and Chemistry Laboratory, Mianyang 621908, P. R. China; [orcid.org/0000-0002-6965-0621](https://orcid.org/0000-0002-6965-0621)

**Hui Guo** – Beijing National Center for Condensed Matter Physics and Institute of Physics, Chinese Academy of Sciences, Beijing 100190, P. R. China; School of Physical Sciences, University of Chinese Academy of Sciences, Beijing 100190, P. R. China; Hefei National Laboratory, 230088 Hefei, Anhui, P. R. China

**Hao Zhang** – Beijing National Center for Condensed Matter Physics and Institute of Physics, Chinese Academy of Sciences, Beijing 100190, P. R. China; School of Physical Sciences, University of Chinese Academy of Sciences, Beijing 100190, P. R. China

**Guoyu Xian** – Beijing National Center for Condensed Matter Physics and Institute of Physics, Chinese Academy of Sciences, Beijing 100190, P. R. China; School of Physical Sciences, University of Chinese Academy of Sciences, Beijing 100190, P. R. China

**Senhao Lv** – Beijing National Center for Condensed Matter Physics and Institute of Physics, Chinese Academy of Sciences,

Beijing 100190, P. R. China; School of Physical Sciences, University of Chinese Academy of Sciences, Beijing 100190, P. R. China

**Guangyuan Han** – Beijing National Center for Condensed Matter Physics and Institute of Physics, Chinese Academy of Sciences, Beijing 100190, P. R. China; School of Physical Sciences, University of Chinese Academy of Sciences, Beijing 100190, P. R. China

**Ruisong Ma** – Beijing National Center for Condensed Matter Physics and Institute of Physics, Chinese Academy of Sciences, Beijing 100190, P. R. China; School of Physical Sciences, University of Chinese Academy of Sciences, Beijing 100190, P. R. China

**Geng Li** – Beijing National Center for Condensed Matter Physics and Institute of Physics, Chinese Academy of Sciences, Beijing 100190, P. R. China; School of Physical Sciences, University of Chinese Academy of Sciences, Beijing 100190, P. R. China; Hefei National Laboratory, 230088 Hefei, Anhui, P. R. China; [orcid.org/0000-0002-3347-7222](https://orcid.org/0000-0002-3347-7222)

**Chengmin Shen** – Beijing National Center for Condensed Matter Physics and Institute of Physics, Chinese Academy of Sciences, Beijing 100190, P. R. China; School of Physical Sciences, University of Chinese Academy of Sciences, Beijing 100190, P. R. China

**Haitao Yang** – Beijing National Center for Condensed Matter Physics and Institute of Physics, Chinese Academy of Sciences, Beijing 100190, P. R. China; School of Physical Sciences, University of Chinese Academy of Sciences, Beijing 100190, P. R. China; Hefei National Laboratory, 230088 Hefei, Anhui, P. R. China

**Qing Huan** – Beijing National Center for Condensed Matter Physics and Institute of Physics, Chinese Academy of Sciences, Beijing 100190, P. R. China; School of Physical Sciences, University of Chinese Academy of Sciences, Beijing 100190, P. R. China

Complete contact information is available at:  
<https://pubs.acs.org/10.1021/acs.nanolett.5c00523>

### Author Contributions

<sup>†</sup>Z.H., H.C., R.S., and H.G. contributed equally to this work. H.-J.G. and H.C. design the experiments. Z.H., H.C., H.Z., G.H., R.M., Q.H., G.L., and C.S. performed the STM/S experiments and data analysis. G.X., H.G., S.L., and H.Y. prepared the AuSn<sub>4</sub> samples. Z.H., H.C., and H.-J.G. wrote the manuscript with input from all other authors. H.-J.G. supervised the project.

### Notes

The authors declare no competing financial interest.

### ACKNOWLEDGMENTS

We thank L. Tao and Y. X. Gao for helpful discussions. The work is supported by grants from the National Natural Science Foundation of China (62488201, 12404188, T2125014), the National Key Research and Development Projects of China (2022YFA1204100, 2022YFA1403103), the CAS Project for Young Scientists in Basic Research (YSBR-003, YSBR-053), the Innovation Program of Quantum Science and Technology (2021ZD0302700), and the Scientific Research Instrument and Equipment Development Project of CAS (PTYQ2024TD0011, PTYO2024BJ0005)

### REFERENCES

- (1) Qi, X. L.; Zhang, S. C. Topological insulators and superconductors. *Rev. Mod. Phys.* **2011**, *83* (4), 1057.
- (2) Kotetes, P. Classification of engineered topological superconductors. *New J. Phys.* **2013**, *15* (10), 105027.
- (3) Zhang, X. M.; Liu, J. L.; Liu, F. Topological Superconductivity Based on Antisymmetric Spin-Orbit Coupling. *Nano Lett.* **2022**, *22* (22), 9000–9005.
- (4) Frolov, S. M.; Manfra, M. J.; Sau, J. D. Topological superconductivity in hybrid devices. *Nat. Phys.* **2020**, *16* (7), 718–724.
- (5) Xu, J. P.; Wang, M. X.; Liu, Z. L.; Ge, J. F.; Yang, X. J.; Liu, C. H.; Xu, Z. A.; Guan, D. D.; Gao, C. L.; Qian, D.; et al. Experimental Detection of a Majorana Mode in the core of a Magnetic Vortex inside a Topological Insulator-Superconductor Bi<sub>2</sub>Te<sub>3</sub>/NbSe<sub>2</sub> Heterostructure. *Phys. Rev. Lett.* **2015**, *114* (1), 017001.
- (6) Palacio-Morales, A.; Mascot, E.; Cocklin, S.; Kim, H.; Rachel, S.; Morr, D. K.; Wiesendanger, R. Atomic-scale interface engineering of Majorana edge modes in a 2D magnet-superconductor hybrid system. *Science Advances* **2019**, *5* (7), No. eaav6600.
- (7) Lo Conte, R.; Wiebe, J.; Rachel, S.; Morr, D. K.; Wiesendanger, R. Magnet-superconductor hybrid quantum systems: a materials platform for topological superconductivity. *Riv. Nuovo Cim* **2025**, na.
- (8) Bihlmayer, G.; Noël, P.; Vyalikh, D. V.; Chulkov, E.; Manchon, A. Rashba-like physics in condensed matter. *Nature Reviews Physics* **2022**, *4* (10), 642–659.
- (9) Manchon, A.; Koo, H. C.; Nitta, J.; Frolov, S. M.; Duine, R. A. New perspectives for Rashba spin-orbit coupling. *Nat. Mater.* **2015**, *14* (9), 871–882.
- (10) Zhang, P.; Yaji, K.; Hashimoto, T.; Ota, Y.; Kondo, T.; Okazaki, K.; Wang, Z. J.; Wen, J. S.; Gu, G. D.; Ding, H.; et al. Observation of topological superconductivity on the surface of an iron-based superconductor. *Science* **2018**, *360* (6385), 182–186.
- (11) Wang, D. F.; Kong, L. Y.; Fan, P.; Chen, H.; Zhu, S. Y.; Liu, W. Y.; Cao, L.; Sun, Y. J.; Du, S. X.; Schneeloch, J.; et al. Evidence for Majorana bound states in an iron-based superconductor. *Science* **2018**, *362* (6412), 333–335.
- (12) Luh, Y. Bound state in superconductors with paramagnetic impurities. *Acta Physica Sinica* **1965**, *21* (1), 75.
- (13) Shiba, H. Classical Spins in Superconductors. *Prog. Theor. Phys.* **1968**, *40* (3), 435.
- (14) Rusinov, A. Theory of gapless superconductivity in alloys containing paramagnetic impurities. *Sov. Phys. JETP* **1969**, *29* (6), 1101–1106.
- (15) Wang, D. F.; Wiebe, J.; Zhong, R. D.; Gu, G. D.; Wiesendanger, R. Spin-Polarized Yu–Shiba–Rusinov States in an Iron-Based Superconductor. *Phys. Rev. Lett.* **2021**, *126* (7), 076802.
- (16) Song, R.; Zhang, P.; He, X. T.; Hao, N. Ferromagnetic impurity induced Majorana zero mode in iron-based superconductors. *Phys. Rev. B* **2022**, *106* (18), L180504.
- (17) Chatzopoulos, D.; Cho, D.; Bastiaans, K. M.; Steffensen, G. O.; Bouwmeester, D.; Akbari, A.; Gu, G.; Paaske, J.; Andersen, B. M.; Allan, M. P. Spatially dispersing Yu–Shiba–Rusinov states in the unconventional superconductor FeTe<sub>0.55</sub>Se<sub>0.45</sub>. *Nat. Commun.* **2021**, *12* (1), 298.
- (18) Fan, P.; Yang, F. Z.; Qian, G. J.; Chen, H.; Zhang, Y. Y.; Li, G.; Huang, Z. H.; Xing, Y. Q.; Kong, L. Y.; Liu, W. Y.; et al. Observation of magnetic adatom-induced Majorana vortex and its hybridization with field-induced Majorana vortex in an iron-based superconductor. *Nat. Commun.* **2021**, *12* (1), 1348.
- (19) Zhai, X.-Y.; Zhao, L. Aurophilic interaction-based aggregation of gem-digold(I) aryls towards high spin-orbit coupling and strong phosphorescence. *Nat. Commun.* **2025**, *16* (1), 405.
- (20) Rybkin, A. G.; Rybkina, A. A.; Otrokov, M. M.; Vilkov, O. Y.; Klimovskikh, I. I.; Petukhov, A. E.; Filianina, M. V.; Voroshnin, V. Y.; Rusinov, I. P.; Ernst, A.; et al. Magneto-Spin-Orbit Graphene: Interplay between Exchange and Spin-Orbit Couplings. *Nano Lett.* **2018**, *18* (3), 1564–1574.

- (21) Zhao, S.; Zhang, H. W.; Zhu, M. F.; Jiang, L. W.; Zheng, Y. S. Electrical conductivity of goldene. *Phys. Rev. B* **2024**, *110* (8), 085111.
- (22) Gumeniuk, R.; Rosner, H.; Schnelle, W.; Nicklas, M.; Leithe-Jasper, A.; Grin, Y. Optimization of the superconducting transition temperature of the filled skutterudite BaPt<sub>4</sub>Ge<sub>12</sub> by gold substitution. *Phys. Rev. B* **2008**, *78* (5), 052504.
- (23) Khasanov, R.; Gupta, R.; Das, D.; Amon, A.; Leithe-Jasper, A.; Svanidze, E. Multiple-gap response of type-I noncentrosymmetric BeAu superconductor. *Physical Review Research* **2020**, *2* (2), 023142.
- (24) Yan, B. H.; Stadtmüller, B.; Haag, N.; Jakobs, S.; Seidel, J.; Jungkenn, D.; Mathias, S.; Cinchetti, M.; Aeschlimann, M.; Felser, C. Topological states on the gold surface. *Nat. Commun.* **2015**, *6* (1), 10167.
- (25) Trivini, S.; Ortuzar, J.; Vaxevani, K.; Li, J. C.; Bergeret, F. S.; Cazalilla, M. A.; Pascual, J. I. Cooper Pair Excitation Mediated by a Molecular Quantum Spin on a Superconducting Proximitized Gold Film. *Phys. Rev. Lett.* **2023**, *130* (13), 136004.
- (26) Xie, Y.-M.; Law, K. T.; Lee, P. A. Topological superconductivity in EuS/Au/superconductor heterostructures. *Physical Review Research* **2021**, *3* (4), 043086.
- (27) Manna, S.; Wei, P.; Xie, Y. M.; Law, K. T.; Lee, P. A.; Moodera, J. S. Signature of a pair of Majorana zero modes in superconducting gold surface states. *Proc. Natl. Acad. Sci. U.S.A.* **2020**, *117* (16), 8775–8782.
- (28) Wei, P.; Manna, S.; Eich, M.; Lee, P.; Moodera, J. Superconductivity in the Surface State of Noble Metal Gold and its Fermi Level Tuning by EuS Dielectric. *Phys. Rev. Lett.* **2019**, *122* (24), 247002.
- (29) Potter, A. C.; Lee, P. A. Topological superconductivity and Majorana fermions in metallic surface states. *Phys. Rev. B* **2012**, *85* (9), 094516.
- (30) Martín-Vega, F.; Herrera, E.; Wu, B.; Barrera, V.; Mompeán, F.; García-Hernández, M.; Canfield, P. C.; Black-Schaffer, A. M.; Baldoví, J. J.; Guillamón, I.; et al. Superconducting density of states and band structure at the surface of the candidate topological superconductor Au<sub>3</sub>Pb. *Physical Review Research* **2022**, *4* (2), 023241.
- (31) Herrera, E.; Wu, B. L.; O’Leary, E.; Ruiz, A. M.; Agueda, M.; Talavera, P. G.; Barrera, V.; Azpeitia, J.; Munuera, C.; García-Hernández, M.; et al. Band structure, superconductivity, and polytypism in AuSn<sub>4</sub>. *Physical Review Materials* **2023**, *7* (2), 024804.
- (32) Karn, N. K.; Sharma, M. M.; Awana, V. P. S. Non-trivial band topology in the superconductor AuSn<sub>4</sub>: a first principle study. *Superconductor Science & Technology* **2022**, *35* (11), 114002.
- (33) Sharma, M. M.; Rani, P.; Awana, V. P. S. Probing the topological surface states in superconducting Sn<sub>4</sub>Au single crystal: a magneto transport study. *J. Phys.: Condens. Matter* **2022**, *34* (41), 415701.
- (34) Shen, D.; Kuo, C. N.; Yang, T. W.; Chen, I. N.; Lue, C. S.; Wang, L. M. Two-dimensional superconductivity and magnetotransport from topological surface states in AuSn<sub>4</sub> semimetal. *Communications Materials* **2020**, *1* (1), 56.
- (35) Zhu, W. L.; Song, R.; Huang, J. R.; Wang, Q. W.; Cao, Y.; Zhai, R. Q.; Bian, Q.; Shao, Z. B.; Jing, H. M.; Zhu, L. J.; et al. Intrinsic surface *p*-wave superconductivity in layered AuSn<sub>4</sub>. *Nat. Commun.* **2023**, *14* (1), 7012.
- (36) Ye, Y. H.; Song, R.; Xiao, H. Q.; Xian, G. Y.; Guo, H.; Yang, H. T.; Chen, H.; Gao, H. J. Visualization of Unconventional Rashba Bands and Vortex Zero Mode in the Topological Superconductor Candidate AuSn<sub>4</sub>. *Nano Lett.* **2024**, *24* (42), 13455–13463.
- (37) Grothe, S.; Chi, S.; Dosanjh, P.; Liang, R. X.; Hardy, W. N.; Burke, S. A.; Bonn, D. A.; Pennec, Y. Bound states of defects in superconducting LiFeAs studied by scanning tunneling spectroscopy. *Phys. Rev. B* **2012**, *86* (17), 174503.
- (38) Madhavan, V.; Chen, W.; Jamneala, T.; Crommie, M. F.; Wingreen, N. S. Tunneling into a single magnetic atom: Spectroscopic evidence of the Kondo resonance. *Science* **1998**, *280* (5363), 567–569.
- (39) Yazdani, A.; Jones, B. A.; Lutz, C. P.; Crommie, M. F.; Eigler, D. M. Probing the local effects of magnetic impurities on superconductivity. *Science* **1997**, *275* (5307), 1767–1770.
- (40) Heinrich, B. W.; Pascual, J. I.; Franke, K. J. Single magnetic adsorbates on *s*-wave superconductors. *Prog. Surf. Sci.* **2018**, *93* (1), 1–19.
- (41) Ménard, G. C.; Guisart, S.; Brun, C.; Pons, S.; Stolyarov, V. S.; Debontridder, F.; Leclerc, M. V.; Janod, E.; Cario, L.; Roditchev, D.; et al. Coherent long-range magnetic bound states in a superconductor. *Nat. Phys.* **2015**, *11* (12), 1013–1016.
- (42) Hatter, N.; Heinrich, B. W.; Ruby, M.; Pascual, J. I.; Franke, K. J. Magnetic anisotropy in Shiba bound states across a quantum phase transition. *Nat. Commun.* **2015**, *6*, 8988.
- (43) Liu, Y.; Li, C.; Xue, F. H.; Su, W.; Wang, Y.; Huang, H. L.; Yang, H.; Chen, J. Y.; Guan, D. D.; Li, Y. Y.; et al. Quantum Phase Transition in Magnetic Nanographenes on a Lead Superconductor. *Nano Lett.* **2023**, *23* (21), 9704–9710.
- (44) Zhang, Y.; Sun, R. J.; Xie, T.; Liu, Z. Y.; Wang, R.; Zhang, W. H.; Liu, C. F.; Fu, Y. S. High-Resolution Spectroscopy of the Intermediate Impurity States near a Quantum Phase Transition. *Nano Lett.* **2024**, *24* (45), 14222–14228.
- (45) Anderson, P. W. Localized magnetic states in metals. *Phys. Rev.* **1961**, *124* (1), 41.
- (46) Yu, L.; Hu, L.; Barreda, J. L.; Guan, T.; He, X.; Wu, K.; Li, Y.; Xiong, P. Robust Gapless Surface State against Surface Magnetic Impurities on (Bi<sub>0.5</sub>Sb<sub>0.5</sub>)<sub>2</sub>Te<sub>3</sub> Evidenced by In Situ Magnetotransport Measurements. *Phys. Rev. Lett.* **2020**, *124* (12), 126601.
- (47) Kresse, G.; Furthmüller, J. Efficient iterative schemes for ab initio total-energy calculations using a plane-wave basis set. *Phys. Rev. B* **1996**, *54* (16), 11169–11186.
- (48) Kresse, G.; Joubert, D. From ultrasoft pseudopotentials to the projector augmented-wave method. *Phys. Rev. B* **1999**, *59* (3), 1758–1775.
- (49) Blöchl, P. E. Projector augmented-wave method. *Phys. Rev. B* **1994**, *50* (24), 17953–17979.
- (50) Perdew, J. P.; Burke, K.; Ernzerhof, M. Generalized Gradient Approximation Made Simple. *Phys. Rev. Lett.* **1996**, *77* (18), 3865–3868.
- (51) Grimme, S.; Antony, J.; Ehrlich, S.; Krieg, H. A consistent and accurate ab initio parametrization of density functional dispersion correction (DFT-D) for the 94 elements H-Pu. *J. Chem. Phys.* **2010**, *132* (15), 154104–154123.